Enhancing the Thermoelectric Properties of Conjugated Polymers by Suppressing Dopant-Induced Disorder

Suhao Wang,* Wenjin Zhu, Ian E. Jacobs, William A. Wood, Zichen Wang, Suraj Manikandan, Jens Wenzel Andreasen, Hio-Ieng Un, Sarah Ursel, Sébastien Peralta, Shaoliang Guan, Jean-Claude Grivel, Stéphane Longuemart, and Henning Sirringhaus*

Doping is a crucial strategy to enhance the performance of various organic electronic devices. However, in many cases, the random distribution of dopants in conjugated polymers leads to the disruption of the polymer microstructure, severely constraining the achievable performance of electronic devices. Here, it is shown that by ion-exchange doping polythiophene-based P[(3HT)$_{1-x}$-stat-(T)$_x$] ($x = 0$ (P1), 0.12 (P2), 0.24 (P3), and 0.36 (P4)), remarkably high electrical conductivity of >400 S cm^{-1} and power factor of >16 µW m^{-1} K^{-2} are achieved for the random copolymer P3, ranking it among highest ever reported for unaligned P3HT-based films, significantly higher than that of P1 (<40 S cm^{-1}, <4 µW m^{-1} K^{-2}). Although both polymers exhibit comparable field-effect transistor hole mobilities of ≈ 0.1 cm^2 V^{-1} s^{-1} in the pristine state, after doping, Hall effect measurements indicate that P3 exhibits a large Hall mobility up to 1.2 cm^2 V^{-1} s^{-1}, significantly outperforming that of P1 (0.06 cm^2 V^{-1} s^{-1}). GIWAXS measurement determines that the in-plane π–π stacking distance of doped P3 is 3.44 Å, distinctly shorter than that of doped P1 (3.68 Å). These findings contribute to resolving the long-standing dopant-induced-disorder issues in P3HT and serve as an example for achieving fast charge transport in highly doped polymers for efficient electronics.

1. Introduction

Doping of conjugated polymers is one of the most important milestones during the preceding four decades in the field of organic electronics and its significance was acknowledged by the Nobel Prize in Chemistry in 2000.[1] In addition to acting as an enabler in conventional organic electronics such as organic solar cells (OSCs),[2] organic field-effect transistors (OFETs),[3] and organic light-emitting diodes,[4] the interests in doping of conjugated polymers have been further sparked by emerging applications,[5] such as thermoelectrics,[6] sensing,[7] and bioelectronics.[8] Despite these advances and widespread applications, a long-lasting challenge, that has been limiting the achievable performance of various electronic devices, is the trade-off between achieving a high doping level and minimizing dopant-induced structural disorder in the doped films. Recent experimental and theoretical investigations suggest structural disorder, rather than Coulomb trapping, is what limits charge transport and ultimate conductivities.[9] Thus, the limiting factor for electronic devices in doped polymers is not carrier density, but carrier mobility. However, research on minimizing structural disorder and maximizing charge carrier mobility in the doped state is still rarely reported, and the charge-transport mechanism in highly doped polymers is still poorly understood.

S. Wang, W. Zhu, I. E. Jacobs, W. A. Wood, Z. Wang, H.-I. Un, S. Ursel, H. Sirringhaus
Optoelectronics Group
Cavendish Laboratory
JJ Thomson Avenue, Cambridge CB3 0HE, UK
E-mail: suhao.wang@univ-littoral.fr; hs220@cam.ac.uk
S. Wang, S. Longuemart
Unité de Dynamique et Structure des Matériaux Moléculaires
Université du Littoral Côte d'Opale
145 Avenue Maurice Schumann, Dunkerque 59140, France

The ORCID identification number(s) for the author(s) of this article can be found under https://doi.org/10.1002/adma.202314062

S. Manikandan, J. W. Andreasen, J.-C. Grivel
Department of Energy Conversion and Storage
Technical University of Denmark
Kongens Lyngby 2800, Denmark
S. Peralta
Laboratoire de Physicochimie des Polymères et des Interfaces
CY Cergy Paris Université
5 Mail Gay Lussac, Neuville-sur-Oise 95000, France
S. Guan
Maxwell Centre
Cavendish Laboratory
University of Cambridge
Cambridge CB3 0HE, UK

**ADVANCED
SCIENCE NEWS**

www.advancedsciencenews.com

**ADVANCED
MATERIALS**

www.advmat.de
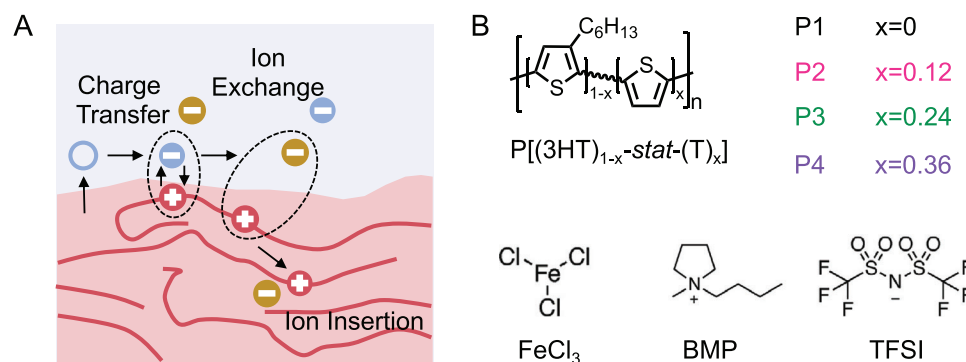
Figure 1. A) Schematic illustration of ion-exchange doping process, and B) molecular structures of P[(3HT)$_{1-x}$-stat-(T)$_x$], BMP, TFSI, and FeCl$_3$.

Because the microstructure of the doped polymer films plays a critical role in determining the optoelectronic characteristics,[10] it is important to adopt appropriate doping techniques for conjugated polymers.[6f,11] Recently, a newly developed ion-exchange (IEx) doping method has been recognized as an ideal testbed for the realization of high-performance conducting polymers and understanding the underpinning structure–property relationships.[12] Different from conventional molecular doping, IEx doping is based on the doping of a solid-state polymer film with a solution that contains both a molecular dopant and an electrolyte. During IEx doping, after charge transfer from the polymer onto the molecular dopant, the ionized molecular dopant is exchanged for a stable, closed-shell ion, which finally serves as a stable counterion. (**Figure 1A**) IEx doping not only prevents the formation of fractional charge transfer complex and unstable radical ions, which are often formed in conventional molecular doping, limit the achievable conductivity and induce degradation but also allows for a considerably wider choice of ions from a variety of commercially available ionic liquids/salts.[12c] Furthermore, it is also in essence a sequential doping approach that helps minimize the disruption to the polymer microstructure after doping.[13]

Poly-3-hexyl-thiophene (P3HT) is a conjugated polymer model system, that has been widely studied for applications in OFETs.[14] Compared to thiophene-based copolymers, such as poly[2,5-bis(3-tetradecylthiophen-2-yl)thieno[3,2-b]thiophene] (PBTTT), the side chain density of P3HT is high and the side chains do not interdigitate.[15] In IEx-doped films of PBTTT the layer of interdigitated side chains expands and a well-defined molecular cavity opens up to accommodate the dopant counterions; this results in doped films retaining a very high level of crystallinity. Highly doped films of PBTTT tend to exhibit lower paracrystallinity values (<8%) than undoped films and achieve very high conductivities >1000 S cm^{-1}.[12c,16] In contrast, doping-induced disorder is more pronounced in P3HT; doped films tend to exhibit significantly higher paracrystallinity values than undoped films and conductivities are typically limited to <100 S cm^{-1}, in most cases <10 S cm^{-1}.[17] Recently, several reports demonstrated that side chain density engineering is an effective approach to improve the intermolecular packing and enhance the electrical properties of both pristine and doped polymer films.[18] In the present work, we report for the first time the IEx doping of a family of regioregular P3HT-based random co-polymers, P[(3HT)$_{1-x}$-stat-(T)$_x$] containing dif-

ferent proportions of unsubstituted thiophene units ($x = 0$ (P1, i.e., P3HT, $M_w = 27.3$ kDa, PDI = 1.63), 0.12 (P2, $M_w = 27.2$ kDa, PDI = 1.62), 0.24 (P3, $M_w = 28.0$ kDa, PDI = 1.67), and 0.36 (P4, $M_w = 28.2$ kDa, PDI = 1.65)). Our original idea in the present work was to enhance interchain interactions to create well-defined molecular cavities in the random copolymers, in which the dopant counterions can be incorporated without causing pronounced structural disorder. To dope the co-polymers by IEx doping, we used FeCl$_3$ as a molecular dopant and BMP-TFSI in acetonitrile as the electrolyte. We show that both π–π stacking and side-chain packing of the doped polymer films reach an optimal level with minimized structural disorder in the case of P3 and that doped P3 exhibits the highest electrical conductivities in excess of 400 S cm^{-1}, compared to that of doped P3HT/P1(<40 S cm^{-1}). We present a careful discussion of the origin of this surprising improvement in conductivity on the basis of optical spectroscopy, X-ray measurements, microstructural characterization, and Hall effect measurements.

2. Results and Discussion

We first evaluated the charge transport properties of the pristine polymers using top-gate bottom-contact (TGBC) OFETs. As shown in Figure S1 (Supporting Information), P1, P2 and P3 all have similar hole mobilities of ≈0.1 cm^2 V^{-1} s^{-1}, ((0.08 ± 0.001) cm^2 V^{-1} s^{-1} for P1, (0.084 ± 0.005) cm^2 V^{-1} s^{-1} for P2, and (0.136 ± 0.025) for P3) that are typical for high quality P3HT films, whereas P4 has slightly lower mobility ((0.028 ± 0.005) cm^2 V^{-1} s^{-1}). Because the field-effect mobility is highly sensitive to polymer microstructure, these results already suggest that P1, P2, and P3 have similarly ordered microstructures. To gain insights into the origin of the comparable mobilities of these polymers, we then measured photothermal deflection spectroscopy (PDS), which probes the energetic disorder in the joint density of states due to sub-bandgap tail states.[19] As shown in Figure S2 (Supporting Information), all pristine polymers exhibit strong sub-bandgap absorption at energies below 1.7 eV, which could arise due to a combination of polymer aggregation and polaron-induced absorptions due to residual doping, for example due to oxygen exposure. The inserted figure in Figure S2 (Supporting Information) displays the calculated values of Urbach energy for all the polymers. Note that these extracted values of the Urbach energy may not reflect the real situation of the energetic ordering since the slopes of the linear regime

**ADVANCED
SCIENCE NEWS**

www.advancedsciencenews.com

**ADVANCED
MATERIALS**

www.advmat.de
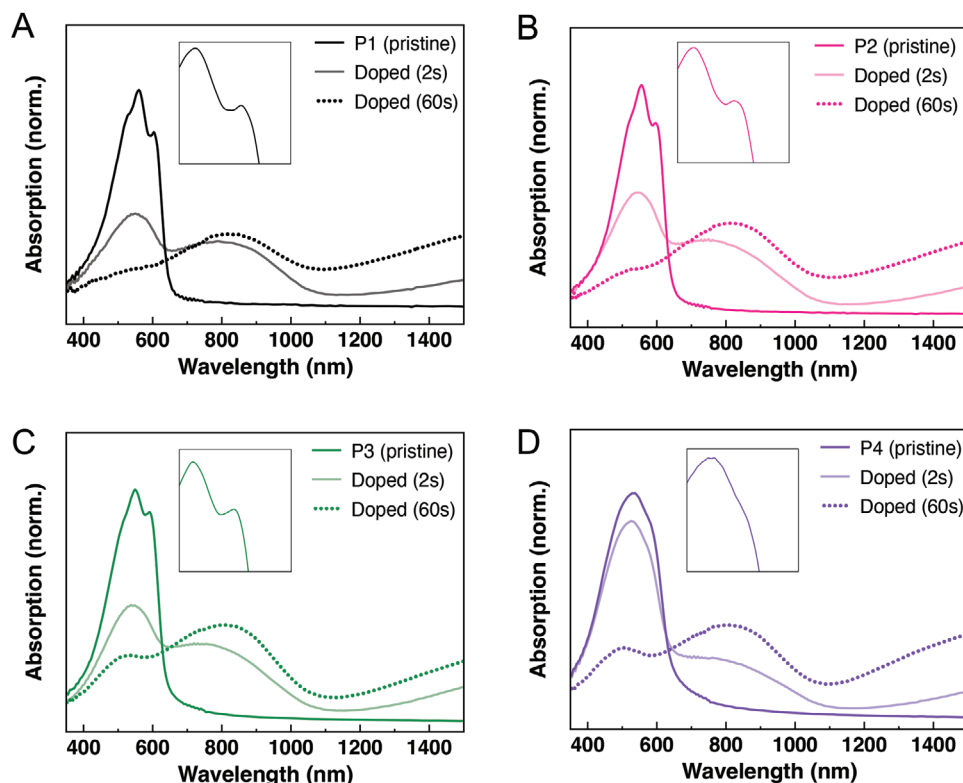
Figure 2. UV–vis–NIR spectra of A) P1, B) P2, C) P3, and D) P4, with the doping time of 0, 2, and 60 s, respectively.

are influenced by the quite intense absorbance in the tail regime (<1.8 eV) due to aggregation and/or air doping. Note all the polymers have comparable ionization energy (IE) values, all ranging between −4.9 and −5.0 eV (IESS: −4.94 eV for P1; −4.97 for P2; −4.91 eV for P3; −5.00 for P4), thus the different sub-bandgap absorption is most likely dictated by their different air doping level to the polymer chains. The argument of the increased unsubstituted thiophene rings and the stronger chain stacking is actually consistent with the gradually more visible residual absorbance peak of the pristine polymer chains at ≈500 nm as observed in **Figure 2A–D**. Note the P3HT that is used in the current study has lower M_w and lower PDI than that of the commonly used commercial P3HT. Previous studies showed that both M_w and PDI have a non-negligible impact on the solid-state microstructures of polymer films.[20]

IEx doping was performed by covering the solid-state polymer films with 100 µL of 1 mM/100 mM FeCl$_3$/BMP-TFSI in acetonitrile solution and keeping the solution in contact with the film for a variable delay period ranging from 2 to 100 s before spinning off the excess. During the spinning, 1 mL of acetonitrile was dropped on the spinning doped films to remove electrolyte and FeCl$_3$ from the doped film surface. The optical properties of all polymer films before and after IEx doping were investigated by UV–vis–NIR absorption spectroscopy. As is shown in Figure 2A–C, the pristine polymers of P1, P2, and P3 all exhibit pronounced vibrational progressions (see the shoulder in the inserted zooming-in figures), indicating substantial levels of intermolecular aggregations as suggested by Spano et al.[21] In comparison, the vibrational progression is weaker in the case of P4,

(Figure 2D) suggesting a reduced extent of intermolecular aggregations, which is consistent with its slightly lower hole mobilities. For all four polymers, the π–π^* band at ≈540 nm is continuously bleached with the doping time increasing from 2 to 60 s while the polaron-induced absorption band at ≈820 nm increases. At the doping time of 60 s, the neutral absorption band almost disappears for all polymers, indicating a high doping level without remaining neutral chains and probable formation of bipolaron or multipolaron states, as previously observed in electrochemically doped P3HT films and IEx doped PBTTT films.[12c,22] While the residual π–π^* absorption is slightly higher in doped P3 and P4, the similar peak intensity of the polaron-induced absorption band for all polymers indicates a similarly high doping level for P1, P2, P3, and P4.

The in-plane electrical conductivity of the doped polymers was measured for different doping times ranging from 2 to 100 s. As shown in **Figure 3A**, with the doping time increasing, the electrical conductivity first increases, and then reaches a saturated level for P1 and P2 at the doping time of ≈40s, whereas for P3 and P4 it keeps increasing after the doping time of 60 s. Finally, the maximum electrical conductivity for doped P3 is achieved at 100 s, reaching 437.0 (±57.3) S cm^{-1}, over 10 times higher than that of doped P1 of 34.1 (±4.1) S cm^{-1}. Figure 3B displays the maximum electrical conductivity for each polymer. To evaluate the thermoelectric performance of the polymers, the Seebeck coefficient of the doped polymers was measured as well. As shown in Figure 3C, all four polymers show similar Seebeck coefficient values and a similar decreasing trend with increased doping time. The resulting power factor of all the polymers was calculated
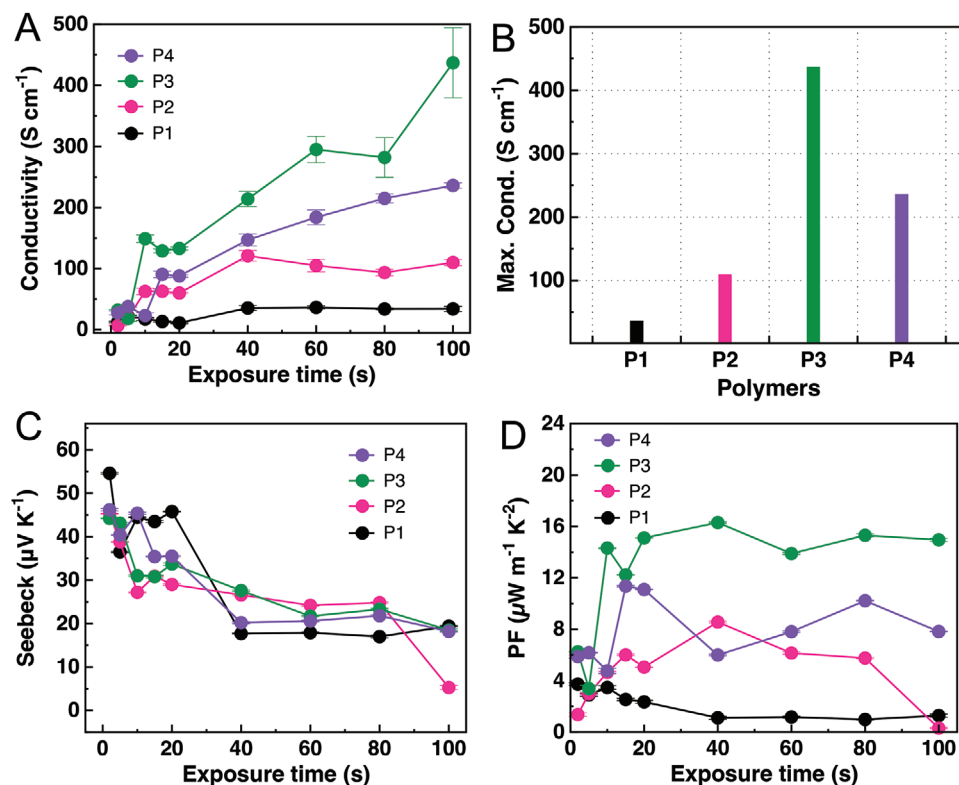
Figure 3. A) Exposure time-dependent electrical conductivity B) Maximum electrical conductivity, C) Exposure time-dependent Seebeck coefficient, and D) the exposure time-dependent power factor of the four doped polymers.

and shown in Figure 3D. Remarkably, doped P3 reaches the maximum power factor of 16.3 ($\pm$0.06) μW m^{-1} K^{-2}, in comparison to 3.7 ($\pm$0.10), 8.6 ($\pm$0.07) and 10.2 ($\pm$0.04) μW m^{-1} K^{-1} for doped P1, P2 and P4, respectively. It is known that TFSI allows for a more efficient doping than FeCl$_3$. We performed FeCl$_3$ doping on the random copolymer P3 and measured the electrical conductivity of the FeCl$_3$-doped films after exposing the films for 2, 20, 60, and 100 s. As shown in Figure S4 (Supporting Information), the maximum conductivity values of the FeCl$_3$-doped films were recorded at the exposure time of 100 s, reaching 148.4 ($\pm$25.6) S cm^{-1}, approximately three times lower than that of the BMP-TFSI-doped P3.

The pristine and IEx-doped polymer films were subjected to atomic force microscopy (AFM) (Figure S5, Supporting Information), and no discernible morphological differences were observed. The solid-state microstructure of the pristine and doped polymers was further investigated using 2D Grazing-incidence wide-angle X-ray scattering (GIWAXS), and the results are displayed in **Figures 4**, **S6** (Supporting Information), and **Table 1**. As shown in the 2D diffraction patterns in the top row of Figure 4A, all pristine polymers display lamellar packing, with the polymer backbone typically oriented edge-on. The GIWAXS pattern of the P1, P2, and P3 film shows considerable long-range crystallinity with both well-ordered out-of-plane peaks (h00) and in-plane stacking peaks being clearly visible. For pristine films, the coherence lengths extracted from the width of π–π stacking diffraction (Table 1) are similar for P1 – P3 and reduced in P4. After IEx doping, the same trend is observed. Notably, both π–π stacking and

lamellar stacking distances decrease from P1 to P3, as shown in Figure 4B,C and Table 1. After IEx doping, the π–π stacking distance generally decreases for all the polymers (Figure 4B), with P1 decreasing from 3.85 to 3.65 Å, and P3 from 3.67 to 3.44 Å. The significantly closer backbones of doped P3 naturally facilitate much faster charge transport, well explaining the much higher conductivity of >400 S cm^{-1} and much larger thermoelectric power factor of 16.3 μW m^{-1} K^{-2} (Figure 3). Hereby, the shortening of the pi–pi stacking d-spacing is attributed to the polaronic coupling between the chains. In fact, as previously suggested, without the actual existence of any dopant molecules, polaron delocalization between neighboring chains results in attractive forces that shorten the π–π stacking distance.[23] Notably, recent studies demonstrate that although long-range crystallinity seems not necessary in aggregating polymers,[24] due to the fact that the mean free path of charges in the π-stacks is as short as ≈1nm,[25] the shorter π–π distances do facilitate better molecular orbital overlap and thus more efficient charge transport.[26] For instance, as Bao and coworkers reported, by bringing the polymer backbones closer, that is reducing the π–π stacking distance from 3.76 to 3.58 Å in an isoindigo-based conjugated polymer, the charge carrier mobility increased from 0.30 up to 2.0 cm^2 V^{-1} s^{-1}.[26a] On the other hand, the lamellar spacing generally expands for all the polymers upon IEx doping (Figure 4C), a clear-cut signature that the counterions mainly reside in the alkyl side-chain zones, which is in line with previous findings on P3HT and PBTTT.[9a,17c] Taken together, the evolution of the GIWAXS indicates that dopants primarily inhabit the side-chain region and

**ADVANCED
SCIENCE NEWS**

www.advancedsciencenews.com

**ADVANCED
MATERIALS**

www.advmat.de
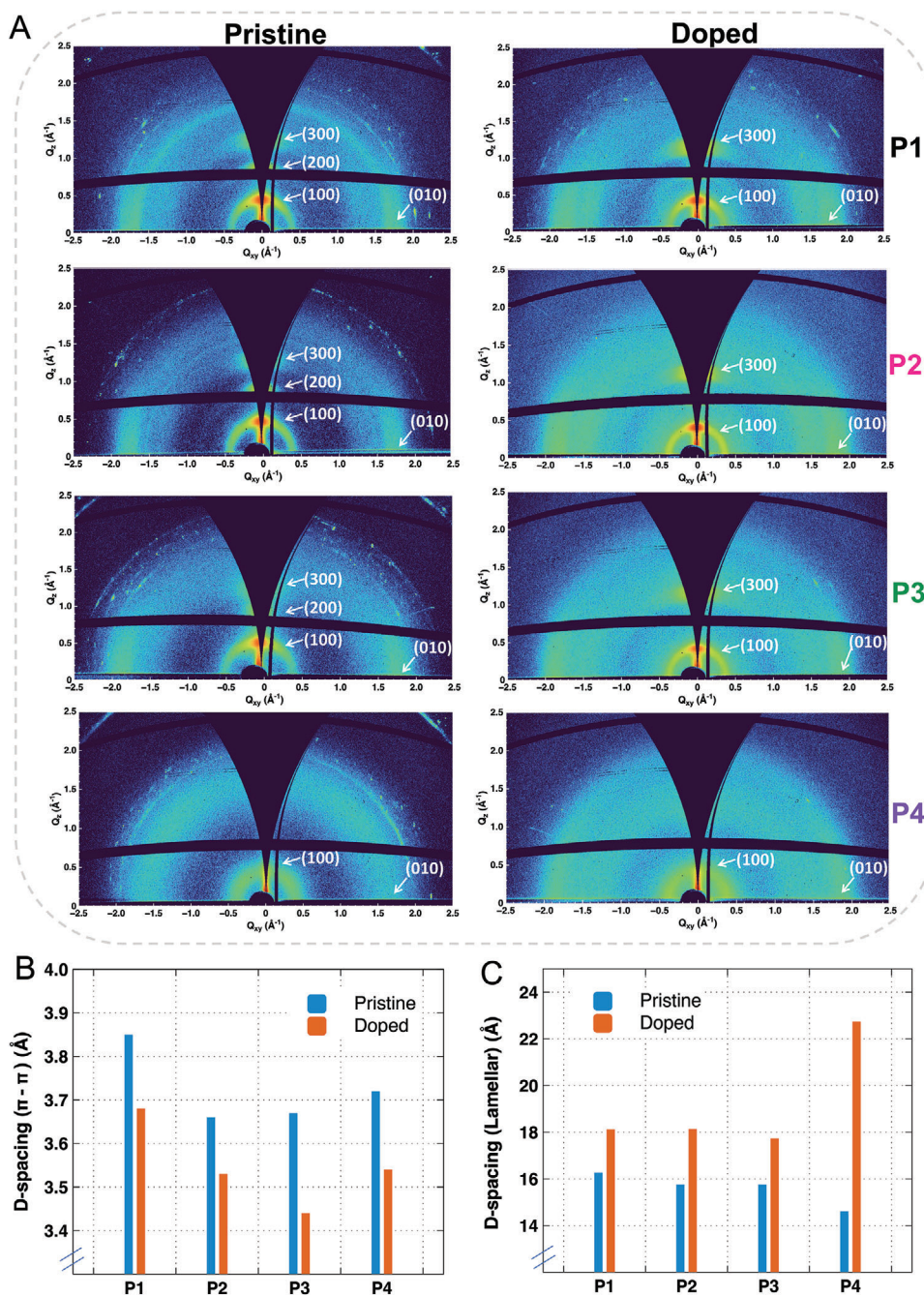
Figure 4. A) 2D GIWAXS patterns of pristine (left row) and ion-exchanged doped (right row) polymer thin films. B) $\pi-\pi$ stacking distances in q_{xy} direction for the pristine and doped polymers. C) lamellar packing distances in q_z for the pristine and doped polymers.

the IEx doping enhances the planarization of the backbone, thus facilitating charge transport in the doped films, especially of the random copolymer P3.

We performed survey scans of the X-ray photoelectron spectroscopy (XPS) spectra of ion-exchange doped P1 and P3(both at the exposure time of 60 s). From **Figure 5A,B**, we can see clearly that there are neither Cl2p peaks at ≈200 eV nor Fe2p peaks at ≈710 eV. Instead, we observe the F1s peaks at ≈690 eV and S2p peaks at ≈170 eV. This is clear evidence of the success of

ion-exchange doping. We additionally performed a more detailed analysis of the S2p region, which allows us to quantify the doping level in the IEx-doped P1 and P3 films. Although both polymers and TFSI contain sulfur, the difference in charge density leads to the appearance of peaks at different binding energies. As shown in Figure 5, the XPS spectra for P1(Figure 5C) and P3 (Figure 5D) show a strong signal with a maximum at 168.4 eV. This is evidence that TFSI has efficiently been doped into the film. Fitting with two doublets yields a very good agreement with the

ADVANCED
SCIENCE NEWS

www.advancedsciencenews.com

ADVANCED
MATERIALS

www.advmat.de

Table 1. GIWAXS quantitative data of all the polymers.

Polymers	Lamellar packing				$\pi-\pi$ stacking			
	d[Å]pr	CL[Å]pr	d[Å]do	CL[Å]do	d[Å] pr	CL[Å] pr	d[Å]do	CL[Å]do
P1	16.3	121	18.1	133	3.85	14	3.68	15
P2	15.8	126	18.1	147	3.66	18	3.53	16
P3	15.8	132	17.7	118	3.67	16	3.44	17
P4	14.6	92	22.7	167	3.72	14	3.54	16

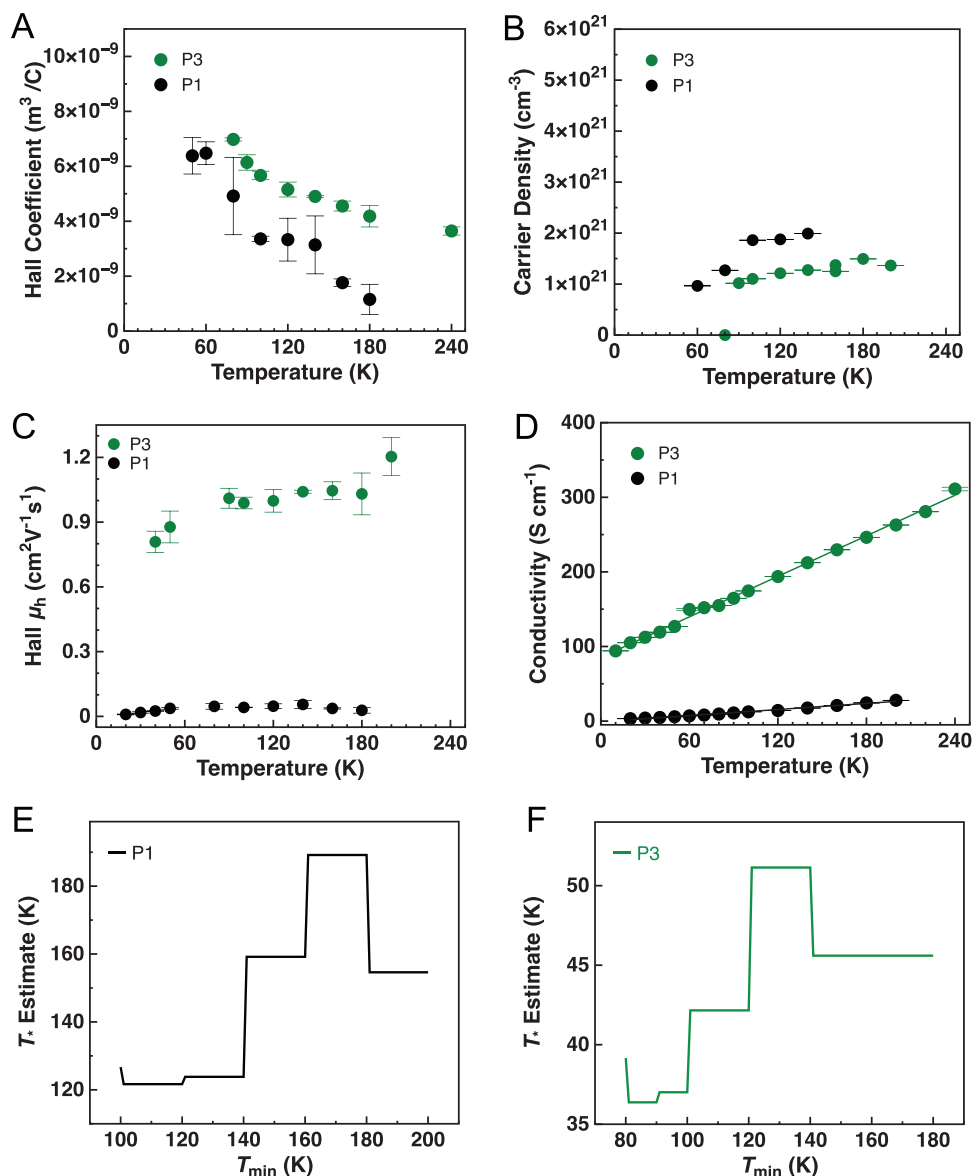d- means d-spacing, CL- means coherent length, pr means pristine, do means doped (exposure time: 60s).

measured signal for the polymers between 161 and 167 eV, which is attributable to an increased binding energy for polarons. The TSFI dopant requires only one set of peaks for fitting, indicating both S atoms on the molecule are chemically equivalent. Details for the fitting is shown in SI. By computing the areas of the peaks originating from the polymers (between 161 and 167 eV) and comparing them with those of the peaks from the TFSI ions (between 167 and 172 eV), the sulfur atomic ratio of TSFI to a polymer can be estimated. Consequently, the doping level is calculated to be 11% for P1, and 15% for P3, where doping level is defined as the number of TFSI ions per thiophene ring. These values are consistent with previously reported maximum doping levels in P3HT, which range between 13% and 17%.[9a,17a,27]

To shed further light on the effect of ion-exchange doping on the charge transport properties we performed Hall measurements (see Supporting Information); for these, we focused on a comparison of P1 and P3. As shown in **Figure 6A**, the measured Hall coefficient of both P1 and P3 decreases with increasing temperature. The carrier density p (Figure 6B) extracted by assuming an ideal Hall response ($R_H = 1/(p \times e)$) is very high; it is comparable to one charge per repeat unit of the polymer backbone, that is, a carrier concentration of $\approx 2 \times 10^{21}$ cm^{-3}. The carrier concentration of doped P1 is slightly higher than that of doped P3. The corresponding Hall mobility of P1 reached ≈ 0.055 (± 0.019) cm^2 V^{-1} s^{-1}, whereas this value for P3 is 20 times higher, reaching up to 1.2 (± 0.09) cm^2 V^{-1} s^{-1} (Figure 6C). Figure 6D displays the temperature-dependent conductivity of doped P1 and P3, indicating that in both films the charge transport is thermally activated. From 20K to 200K, the electrical conductivity of P1 increased from 3.2 to 27.8 S cm^{-1} (by a factor of 8.7), whereas the conductivity of P3 increased from 105.0 to 262.8 S cm^{-1} (by a factor of 2.5), implying much stronger temperature-dependence of P1. Indeed, as shown in Figure S9 (Supporting Information), the activation energy E_a of doped P3 is distinctly lower than that of P1: Between 100–200 K, E_a is 16.3 (± 1.1) meV for P1 and 8.98 (± 0.63) meV for P3;
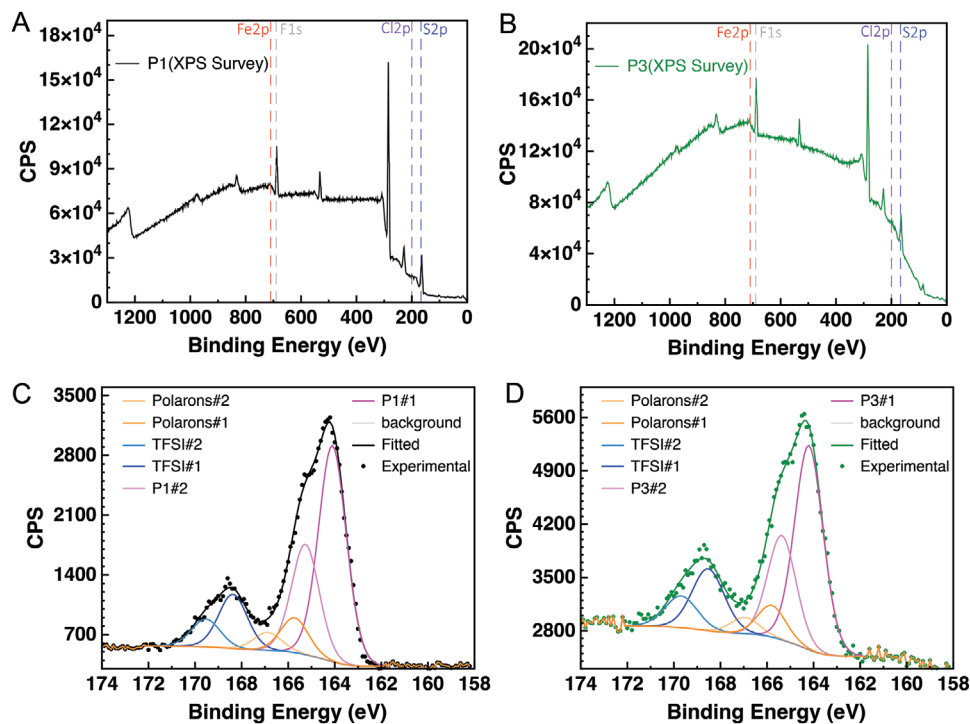
Figure 5. Survey scans of the XPS spectra of IEx-doped P1(A) and P3(B). Sulfur 2p XPS spectra of IEx-doped P1(C), and P3 (D) (60 s exposure time, BMP TFSI/FeCl$_3$).

ADVANCED
SCIENCE NEWS

www.advancedsciencenews.com

**ADVANCED
MATERIALS**

www.advmat.de

Figure 6. Plots of temperature-dependent data acquired from the IEx-doped Hall bar devices of P1 and P3, A) Hall coefficient, and B) carrier density, C) Hall mobility, D) conductivity and estimates of T∗ for different threshold values of temperature for E) P1, and F) P3.

between 50K–100K, E_a reduces to 4.84 ($\pm$0.24) meV for P1 and 0.84 ($\pm$0.16) meV for P3.

On the other hand, the pronounced temperature dependence of the Hall coefficient, which is similar to that previously reported for PBTTT,[24] indicates that the Hall effect in our polymers may be affected by screening effects from localized carriers. These exhibit a thermally activated transport and are either not deflected by the magnetic field (while undergoing hopping), or whose deflection is partially frustrated (during quasi-1D transport). Such carriers diminish the measured Hall coefficient because they do not contribute to the generation of the Hall voltage, but screen the Hall voltage that is generated by more delocalized carriers. As temperature is increased, the mobility of localized carriers increases and their contribution to overall conduction increases, leading to a greater suppression of the Hall coefficient.

We can use our previously proposed model[28] to interpret the Hall coefficient more quantitatively in this regime:

$$R_H(T) = \frac{1}{qn_d}\left[1 + h\exp\left\{-\left(\frac{T_*}{T}\right)^D\right\}\right]^{-2} \qquad (1)$$

where $\langle n_d \rangle$ is the average density of "deflectable" carriers (i.e., carriers that respond to magnetic fields fully as a free charge would), T_* is a variable-range-hopping-like coefficient that characterizes the transport of the localized carriers and is related to the energetic disorder of disordered regions of the polymer, D is a variable-range-hopping-like dimensionality parameter, and h is a parameter that reflects the ratio of the conductivity from nondeflectable and deflectable carriers when $T \gg T_*$.

**ADVANCED
SCIENCE NEWS**

www.advancedsciencenews.com

**ADVANCED
MATERIALS**

www.advmat.de

These parameters can be determined by a careful fitting routine, that has been detailed in the previous report.[28] Of particular interest is the parameter T_*, as it should shed some light onto the relative degree of energetic disorder in both systems. This is because T_* controls how quickly the Hall coefficient saturates with temperature, with a smaller value indicating that contributions from incoherent transport saturate at lower temperatures. As such, a smaller value of T_* can be argued to imply a lesser amount of energetic disorder.

As shown in our previous report[28] (and in the Supporting Information), T_* can be estimated without performing a full fit of the data. However, this estimate will be an underestimate if not in the correct temperature limit. Therefore, a cut-off temperature is defined, T_{min}, as being the temperature value below which data points are excluded from the estimation. As can be seen in Figure 6E,F, the maximum estimate of T_* for the P3 device is ≈55 K, whereas it is ≈190 K for P1. The ranges of their estimates do not overlap, with both exhibiting a minimum value roughly equal to 70% of their maximum values. As such, it is reasonable to assume that while we might not be in the limit required to calculate T_* accurately, we are comparably far away from the said limit in both cases. As such, this (potential) underestimate of T_* for P1 being greater than that for P3 implies that the true values of T_* have a similar ordering (i.e., that $T_*^{P1} > T_*^{P3}$), suggesting a lower degree of energetic disorder in P3 than in P1, consistent with the conclusions drawn from comparing Hall mobilities. Taking together the conductivity measurement in Figure 3 and Hall results in Figure 6, the greatly improved electrical conductivity of doped P3 can be attributed to its more energetically ordered landscape, thus enabling greater charge-carrier mobilities. The lower carrier concentration in P3 than in P1 could be attributed to the closer stacked polymer chains.

Since environmental stability is a crucial concern for industrial applications, we evaluated the ambient stability of the IEx-doped random copolymer P3 (doping time of 60 s). As shown in Figure S11 (Supporting Information), when exposing the doped films to air, the electrical conductivity dropped from ≈300 to ≈220 S cm^{-1} after 30 min and further decreased to ≈205 S cm^{-1} after 1h. Then it dropped to ≈137 S cm^{-1} upon exposure to air for 24 h. After 24 h, the conductivity remains nearly invariant despite longer exposure, with only a slight decrease, remaining higher than 120 S cm^{-1} after 120 h in the air.

3. Conclusion

The energetically ordered landscape was achieved in highly IEx-doped polythiophene-based random copolymer P[(3HT)$_{0.76}$-stat-(T)$_{0.24}$] (P3) films, leading to high Hall mobility of up to 1.2 cm^2 V^{-1} s^{-1} and high electrical conductivity of >400 S cm^{-1}, significantly outperforming that of benchmark polymer P3HT (P1) (0.06 cm^2 V^{-1} s^{-1} and <40 S cm^{-1}). Moreover, P3 exhibited a high thermoelectric power factor up to 16.3 µW m^{-1} K^{-2}, much higher than that of P1(3.7 µW m^{-1} K^{-2}). GIWAXS measurement indicates that after doping, the in-plane π–π stacking distance of doped P3 is shortened from 3.67 to 3.44 Å, distinctly shorter than that of the doped P1 (3.68 Å), well corroborating the observed high Hall mobility and conductivity. Comprehensive Hall measurement indicates that the doped P3 exhibits much lower activation energy and a lesser amount of energetic disorder. This

work offers an effective strategy to realize fast charge transport in highly doped conjugated polymers and highlights the importance of overcoming dopant-induced disorder in order to achieve next-generation efficient organic electronics.

4. Experimental Section

Preparation of Pristine Polymer Solutions: The polymers were synthesized and the synthetic routes were reported in the literature.[18c,e,26c] Polymer solutions (5 mg mL^{-1}, in chlorobenzene) were heated at 60 °C for 1 h before use. Ion dopant salt solution was prepared at 1 M concentration in acetonitrile. FeCl$_3$ solutions were prepared at 10 mM concentration in acetonitrile. FeCl$_3$ solutions were always prepared immediately before use. All solution preparation processes were performed under a nitrogen atmosphere (<1 ppm of H2O and O2). The polymer solution of 5 g L^{-1} was first spin coated at 1500 rpm for 20 s, and then annealed at 120 °C for 30 mins.

Ion-Exchange Doping: Polymer films were sequentially doped on the spin coater by covering the sample with an electrolyte/FeCl$_3$ solution (100 mM/1 mM in acetonitrile, unless otherwise specified), waiting for a variable delay period (2–100 s) then spinning off the excess. While the sample was still spinning, the doped film was washed with 1 mL of acetonitrile to remove any electrolyte and FeCl$_3$ from the film surface.

OFET Fabrication and Characterization: Top-gate, bottom-contact OFETs (L/W = 20 µm/1000 µm) were fabricated on glass substrates following a procedure of substrate patterning, thermal evaporation of bottom contacts (3 nm Cr and 22 nm Au), polymer spin-coating (parameters described above), Cytop spin-coating (2000 rpm for 20 s, annealing at 90 C for 20 mins, resulting in a thickness of 500 nm) and thermal evaporation of top gate (30 nm of Aluminum). FET characteristics were measured on a Desert TTP4 probe station by an Agilent 4155C Semiconductor Parameter Analyzer. Samples were measured in the glovebox under a nitrogen environment.

AFM Measurements: The surface morphology of polymer films was investigated by atomic force microscopy on Icon coupled at Nanoscope V controller from Bruker in the Tapping mode. The probe was a ScanAsyst Air (Bruker) with a spring constant of 0.4 N m^{-1}.

Electrical Measurements: The in-plane electrical conductivity and Seebeck coefficient measurements were performed on a four-parallel-electrode device architecture (as shown in Figure S3, Supporting Information) by an Agilent 4155B semiconductor parameter analyzer in nitrogen atmosphere (Belle Technology, <10 ppm O2, <20 ppm H2O). Before each measurement, the device was isolated by scratching off the film outside the active device area. The temperature gradient (ΔT) across the sample was imposed by two Peltier modules. The Seebeck coefficient was measured by varying the ΔT across the substrate and measuring the corresponding thermal voltage. Surface profilometry (Bruker DekTak XT) and AFM were used for film thickness determination. More details are provided in the supporting information.

PDS Measurement: PDS was performed using a tunable light source consisting of a 250 W quartz tungsten halogen lamp coupled to a 250 mm focal length grating monochromator. The monochromatic excitation beam was modulated with a mechanical chopper at 13 Hz and focused on the sample surface at a normal incidence angle. The samples were immersed in FluorinertTM FC-72 (3 M) liquid to improve the thermo-optic response in the excitation spot surroundings. The thermal gradient at the sample surface caused by nonradiative relaxation caused the deflection of a probe laser beam passed parallel to the sample surface (transverse configuration), detected by a quadrant photodiode and demodulated with a lock-in amplifier (Stanford Research Systems SR830).

UV–vis Absorption Spectra: UV–vis–NIR spectra were collected on a Shimadzu UV-3600i dual beam spectrometer, with a slit width of 3 nm and a data interval of 1 nm. The background spectra from the blank glass were collected separately.

GIWAXS Measurements: A laboratory setup was used (Xeuss 3.0 from Xenocs S.A.). Here, supplied with a microfocus copper source, Cu Kα radiation (wavelength (λ) = 1.5418 Å) was focused and monochromatized

with a 2D single reflection multilayer optic and collimated with scatterless slits. The silicon substrate surface was aligned at a grazing incident angle of 0.18° with respect to the incoming X-ray beam. The scattered X-rays were detected on an Eiger 4M single-photon counting detector, with 75 μm pixels (DECTRIS), 80.0 mm from the sample. Coherence lengths were determined by application of the Scherrer equation to the FWHM peak widths from fitting the first-order diffraction peaks corresponding to the lamellar stack and pi–pi stack, assuming only size broadening. The analysis of coherence length is somehow limited by the instrumental broadening. The uncertainty of ≈10% in the sample-detector distance results in a peak broadening. Nevertheless, the determination of pi–pi stacking distances is not affected.

XPS Measurements: XPS analysis was performed using a Thermo Scientific Escalab 250Xi fitted with a monochromated Al kα X-ray source (1486.7 eV). All data was recorded with an X-ray beam size of 650 μm, and a pass energy of 20 eV at a step size of 0.1 eV. Electronic charge neutralization was achieved using an ion source. Ion gun current = 100 μA. Ion gun voltage = 40 V. All sample data was recorded at a pressure below 10^{-8} Torr and a room temperature of 294 K. Data was analyzed using CasaXPS v2.3.26rev1.0N. Peaks were fitted with a Shirley background prior to component analysis. A lineshape of GL (30) was used to fit components. Sulfur 2p spectra were characterized by a doublet ($2p_{3/2}$ and $2p_{1/2}$) with a 1:0.511 area ratio and spin–orbit coupling $\Delta = 1.16$ eV.

AC Hall Device Fabrication: For the measurement of the AC Hall, we used the designed Hall bar pattern. The fabrication of the patterned device is as follows: First, the P3HT polymer of 5 g L^{-1} was spin-coated at 1500 rpm for 20 s, then annealed at 120 °C for 30 mins. Then the CYTOP: solvent (1:5 ratio) was spin-coated at 5000 rpm for 90 s and annealed at 80 °C for 20 mins in the glovebox. Then the aluminum oxide film was evaporated with a four-turret evaporator of 1 nm at 0.5 A s^{-1} or less. Then the S1813 was spin-coated at 6000 rpm for 30 s and was baked at 115 °C for 60 s. Then it was mask-aligned and was developed with MF319. Then oxygen plasma for 10 min was carried out to remove the unexpected layer. And finally, the scotch tape was used to detach the extra layers. The patterned AC Hall device was done. More details are provided in the supporting information.

AC Hall Measurement: First, the device adhered to the sample space on the board with the use of GE varnish, followed by the wire bonding to the sample board. Here the device and the samples board were ready for affixing to the sample holder in the cryostat. Then the cryostat was inserted into its vacuum jacket and several hours were waited for the GE varnish to properly cure, followed by evacuating the cryostat. Finally, the internal atmosphere was brought pumped down to ≈10–6 mbar. To carry out the AC Hall measurement, we first use the software PID control to spin up the magnet assembly. Once the frequency of the magnetic field stabilized at the desired value, we waited for another period for the temperature to be stable for at least 15 min. Then the largest current value to be used would be injected to simulate the real conditions where the maximum signal would be found, and the lock-in amplifier was set to auto-range and auto-offset. After this, the current was injected into the device stepping from its lowest value to its highest value. Finally, after performing the vector subtraction and phase optimization, the hall coefficient was determined.

Statistical Analysis: OFET, electrical, and Seebeck coefficient measurements were repeated on three samples and then statistically analyzed to get mean values and SD. The data are presented as mean ± standard deviation (mean ± SD). Origin was used for statistical analysis.

Supporting Information

Supporting Information is available from the Wiley Online Library or from the author.

Acknowledgements

Conflict of Interest

The authors declare no conflict of interest.

Data Availability Statement

The data that support the findings of this study are available from the corresponding author upon reasonable request.

Keywords

[1] a) C. K. Chiang, C. R. Fincher, Y. W. Park, A. J. Heeger, H. Shirakawa, E. J. Louis, S. C. Gau, A. G. MacDiarmid, *Phys. Rev. Lett.* **1977**, *39*, 1098; b) N. Basescu, Z. X. Liu, D. Moses, A. J. Heeger, H. Naarmann, N. Theophilou, *Nature* **1987**, *327*, 403; c) A. D. Scaccabarozzi, A. Basu, F. Aniés, J. Liu, O. Zapata-Arteaga, R. Warren, Y. Firdaus, M. I. Nugraha, Y. Lin, M. Campoy-Quiles, N. Koch, C. Müller, L. Tsetseris, M. Heeney, T. D. Anthopoulos, *Chem. Rev.* **2022**, *122*, 4420.

[2] Y. Zhang, H. Zhou, J. Seifter, L. Ying, A. Mikhailovsky, A. J. Heeger, G. C. Bazan, T.-Q. Nguyen, *Adv. Mater.* **2013**, *25*, 7038.

[3] a) G. Lu, J. Blakesley, S. Himmelberger, P. Pingel, J. Frisch, I. Lieberwirth, I. Salzmann, M. Oehzelt, R. Di Pietro, A. Salleo, N. Koch, D. Neher, *Nat. Commun.* **2013**, *4*, 1588; b) Y. Hu, Z. D. Rengert, C. McDowell, M. J. Ford, M. Wang, A. Karki, A. T. Lill, G. C. Bazan, T.-Q. Nguyen, *ACS Nano* **2018**, *12*, 3938.

[4] P. Zalar, Z. B. Henson, G. C. Welch, G. C. Bazan, T.-Q. Nguyen, *Angew. Chem., Int. Ed.* **2012**, *51*, 7495.

[5] a) L. Ding, Z.-D. Yu, X.-Y. Wang, Z.-F. Yao, Y. Lu, C.-Y. Yang, J.-Y. Wang, J. Pei, *Chem. Rev.* **2023**, *123*, 7421; b) K. Müllen, U. Scherf, *Macromol. Chem. Phys.* **2023**, *224*, 2200337; c) X. Zhu, J. Duan, J. Chen, R. Liu, Z. Qin, H. Chen, W. Yue, *Angew. Chem., Int. Ed.* **2023**, *63*, 202311879.

[6] a) O. Bubnova, X. Crispin, *Energy Environ. Sci.* **2012**, *5*, 9345; b) Y. Chen, Y. Zhao, Z. Liang, *Energy Environ. Sci.* **2015**, *8*, 401; c) B. Russ, A. Glaudell, J. J. Urban, M. L. Chabinyc, R. A. Segalman, *Nat. Rev. Mater.* **2016**, *1*, 16050; d) R. Kroon, D. A. Mengistie, D. Kiefer, J. Hynynen,

J. D. Ryan, L. Yu, C. Muller, *Chem. Soc. Rev.* **2016**, *45*, 6147; e) H. Wang, C. Yu, *Joule* **2019**, *3*, 53; f) W. Zhao, J. Ding, Y. Zou, C. A. Di, D. Zhu, *Chem. Soc. Rev.* **2020**, *49*, 7210; g) M. Massetti, F. Jiao, A. J. Ferguson, D. Zhao, K. Wijeratne, A. Würger, J. L. Blackburn, X. Crispin, S. Fabiano, *Chem. Rev.* **2021**, *121*, 12465; h) S. Wang, G. Zuo, J. Kim, H. Sirringhaus, *Prog. Polym. Sci.* **2022**, *129*, 101548; i) Y. Shi, X. Zhang, T. Du, Y. Han, Y. Deng, Y. Geng, *Angew. Chem., Int. Ed.* **2023**, *62*, 202219262; j) X. Geng, T. Du, C. Xu, Y. Liu, Y. Deng, Y. Geng, *Adv. Funct. Mater.* **2023**, *33*, 2300809.

[7] a) N. Wang, A. Yang, Y. Fu, Y. Li, F. Yan, *Acc. Chem. Res.* **2019**, *52*, 277; b) F. Bonafè, F. Decataldo, I. Zironi, D. Remondini, T. Cramer, B. Fraboni, *Nat. Commun.* **2022**, *13*, 5423; c) A. Koklu, D. Ohayon, S. Wustoni, V. Druet, A. Saleh, S. Inal, *Chem. Rev.* **2022**, *122*, 4581; d) J. Tropp, D. Meli, J. Rivnay, *Matter* **2023**, *6*, 3132; e) P. D. Dongo, A. Hakansson, M.-A. Stoeckel, E. Pavlopolou, S. Wang, D. Farina, P. Queeckers, S. Fabiano, C. S. Iorio, R. Crispin, *Adv. Electron. Mater.* **2023**, *9*, 2300060.

[8] a) T. Someya, Z. Bao, G. G. Malliaras, *Nature* **2016**, *540*, 379; b) D. T. Simon, E. O. Gabrielsson, K. Tybrandt, M. Berggren, *Chem. Rev.* **2016**, *116*, 13009; c) A. Spanu, L. Martines, A. Bonfiglio, *Lab Chip* **2021**, *21*, 795; d) F. Torricelli, D. Z. Adrahtas, Z. Bao, M. Berggren, F. Biscarini, A. Bonfiglio, C. A. Bortolotti, C. D. Frisbie, E. Macchia, G. G. Malliaras, I. McCulloch, K. Moser, T.-Q. Nguyen, R. M. Owens, A. Salleo, A. Spanu, L. Torsi, *Nat. Rev. Methods Primers* **2021**, *1*, 66; e) C. J. Kousseff, R. Halaksa, Z. S. Parr, C. B. Nielsen, *Chem. Rev.* **2022**, *122*, 4397; f) P. C. Harikesh, C.-Y. Yang, H.-Y. Wu, S. Zhang, M. J. Donahue, A. S. Caravaca, J.-D. Huang, P. S. Olofsson, M. Berggren, D. Tu, S. Fabiano, *Nat. Mater.* **2023**, *22*, 242; g) X. Gao, Y. Bao, Z. Chen, J. Lu, T. Su, L. Zhang, J. Ouyang, *Adv. Electron. Mater.* **2023**, *9*, 2300082; h) X. Strakosas, H. Biesmans, T. Abrahamsson, K. Hellman, M. S. Ejneby, M. J. Donahue, P. Ekström, F. Ek, M. Savvakis, M. Hjort, D. Bliman, M. Linares, C. Lindholm, E. Stavrinidou, J. Y. Gerasimov, D. T. Simon, R. Olsson, M. Berggren, *Science* **2023**, *379*, 795.

[9] a) I. E. Jacobs, G. D'Avino, V. Lemaur, Y. Lin, Y. Huang, C. Chen, T. F. Harrelson, W. Wood, L. J. Spalek, T. Mustafa, C. A. O'Keefe, X. Ren, D. Simatos, D. Tjhe, M. Statz, J. W. Strzalka, J.-K. Lee, I. McCulloch, S. Fratini, D. Beljonne, H. Sirringhaus, *J. Am. Chem. Soc.* **2022**, *144*, 3005; b) C. Chen, I. E. Jacobs, K. Kang, Y. Lin, C. Jellett, B. Kang, S. B. Lee, Y. Huang, M. BaloochQarai, R. Ghosh, M. Statz, W. Wood, X. Ren, D. Tjhe, Y. Sun, X. She, Y. Hu, L. Jiang, F. C. Spano, I. McCulloch, H. Sirringhaus, *Adv. Energy Mater.* **2023**, *13*, 2202797.

[10] a) Y. Diao, L. Shaw, Z. Bao, S. C. B. Mannsfeld, *Energy Environ. Sci.* **2014**, *7*, 2145; b) T. Marszalek, M. Li, W. Pisula, *Chem. Commun.* **2016**, *52*, 10938; c) A. Khasbaatar, Z. Xu, J.-H. Lee, G. Campillo-Alvarado, C. Hwang, B. N. Onusaitis, Y. Diao, *Chem. Rev.* **2023**, *123*, 8395; d) L. Deng, Y. Liu, Y. Zhang, S. Wang, P. Gao, *Adv. Funct. Mater.* **2023**, *33*, 2210770; e) G. H. Kim, L. Shao, K. Zhang, K. P. Pipe, *Nat. Mater.* **2013**, *12*, 719; f) Z.-F. Yao, J.-Y. Wang, J. Pei, *Prog. Polym. Sci.* **2023**, *136*, 101626; g) K. A. Peterson, E. M. Thomas, M. L. Chabinyc, *Annu. Rev. Mater. Res.* **2020**, *50*, 551; h) S. Deng, Y. Kuang, C. Liu, X. Liu, J. Liu, J. Li, B. Meng, C.-a. Di, J. Hu, J. Liu, *Adv. Mater.* **2024**, *36*, 2309679.

[11] a) I. E. Jacobs, A. J. Moulé, *Adv. Mater.* **2017**, *29*, 1703063; b) S. E. Yoon, Y. Kang, J. Im, J. Lee, S. Y. Lee, J. Park, Y. J. Gao, D. Jeon, J. Y. Son, J. Kim, C. J. Kousseff, T. Kim, H. Seo, K. Kang, I. McCulloch, S. K. Kwak, H. H. Choi, B.-G. Kim, J. H. Kim, *Joule* **2023**, *7*, 2291; c) Y.-T. Lin, C.-Y. Lee, C.-Y. Wu, J.-M. Lin, T.-C. Lee, S.-H. Tung, C.-L. Liu, *J. Power Sources* **2023**, *556*, 232516; d) J. Tang, Y.-H. Pai, Z. Liang, *ACS Energy Lett.* **2022**, *7*, 4299; e) I. H. Eryilmaz, Y.-F. Chen, G. Mattana, E. Orgiu, *Chem. Commun.* **2023**, *59*, 3160; f) C. Dong, S. Deng, B. Meng, J. Liu, L. Wang, *Angew. Chem., Int. Ed.* **2021**, *60*, 16184.

[12] a) Y. Yamashita, J. Tsurumi, M. Ohno, R. Fujimoto, S. Kumagai, T. Kurosawa, T. Okamoto, J. Takeya, S. Watanabe, *Nature* **2019**, *572*, 634; b) T. L. Murrey, M. A. Riley, G. Gonel, D. D. Antonio, L. Filardi, N. Shevchenko, M. Mascal, A. J. Moulé, *J. Phys. Chem. Lett.* **2021**, *12*,

1284; c) I. E. Jacobs, Y. Lin, Y. Huang, X. Ren, D. Simatos, C. Chen, D. Tjhe, M. Statz, L. Lai, P. A. Finn, W. G. Neal, G. D'Avino, V. Lemaur, S. Fratini, D. Beljonne, J. Strzalka, C. B. Nielsen, S. Barlow, S. R. Marder, I. McCulloch, H. Sirringhaus, *Adv. Mater.* **2022**, *34*, 2102988.

[13] a) D. T. Scholes, S. A. Hawks, P. Y. Yee, H. Wu, J. R. Lindemuth, S. H. Tolbert, B. J. Schwartz, *J. Phys. Chem. Lett.* **2015**, *6*, 4786; b) I. E. Jacobs, E. W. Aasen, J. L. Oliveira, T. N. Fonseca, J. D. Roehling, J. Li, G. Zhang, M. P. Augustine, M. Mascal, A. J. Moulé, *J. Mater. Chem. C* **2016**, *4*, 3454; c) S. Wang, T. P. Ruoko, G. Wang, S. Riera-Galindo, S. Hultmark, Y. Puttisong, F. Moro, H. Yan, W. M. Chen, M. Berggren, C. Muller, S. Fabiano, *ACS Appl. Mater. Interfaces* **2020**, *12*, 53003.

[14] a) Z. Bao, A. Dodabalapur, A. J. Lovinger, *Appl. Phys. Lett.* **1996**, *69*, 4108; b) H. Sirringhaus, P. J. Brown, R. H. Friend, M. M. Nielsen, K. Bechgaard, B. M. W. Langeveld-Voss, A. J. H. Spiering, R. A. J. Janssen, E. W. Meijer, P. Herwig, D. M. de Leeuw, *Nature* **1999**, *401*, 685; c) D. Dudenko, A. Kiersnowski, J. Shu, W. Pisula, D. Sebastiani, H. W. Spiess, M. R. Hansen, *Angew. Chem., Int. Ed.* **2012**, *51*, 11068.

[15] I. McCulloch, M. Heeney, M. L. Chabinyc, D. DeLongchamp, R. J. Kline, M. Cölle, W. Duffy, D. Fischer, D. Gundlach, B. Hamadani, R. Hamilton, L. Richter, A. Salleo, M. Shkunov, D. Sparrowe, S. Tierney, W. Zhang, *Adv. Mater.* **2009**, *21*, 1091.

[16] a) V. Vijayakumar, Y. Zhong, V. Untilova, M. Bahri, L. Herrmann, L. Biniek, N. Leclerc, M. Brinkmann, *Adv. Energy Mater.* **2019**, *9*, 1900266; b) P. Durand, H. Zeng, T. Biskup, V. Vijayakumar, V. Untilova, C. Kiefer, B. Heinrich, L. Herrmann, M. Brinkmann, N. Leclerc, *Adv. Energy Mater.* **2022**, *12*, 2103049.

[17] a) D. T. Duong, C. Wang, E. Antono, M. F. Toney, A. Salleo, *Org. Electron.* **2013**, *14*, 1330; b) E. F. Aziz, A. Vollmer, S. Eisebitt, W. Eberhardt, P. Pingel, D. Neher, N. Koch, *Adv. Mater.* **2007**, *19*, 3257; c) A. Hamidi-Sakr, L. Biniek, J.-L. Bantignies, D. Maurin, L. Herrmann, N. Leclerc, P. Lévêque, V. Vijayakumar, N. Zimmermann, M. Brinkmann, *Adv. Funct. Mater.* **2017**, *27*, 1700173; d) J. Hynynen, D. Kiefer, L. Yu, R. Kroon, R. Munir, A. Amassian, M. Kemerink, C. Muller, *Macromolecules* **2017**, *50*, 8140; e) G. Zuo, Z. Li, O. Andersson, H. Abdalla, E. Wang, M. Kemerink, *J. Phys. Chem. C* **2017**, *121*, 7767; f) E. Lim, K. A. Peterson, G. M. Su, M. L. Chabinyc, *Chem. Mater.* **2018**, *30*, 998; g) J. Guo, Y. Liu, P.-A. Chen, X. Wang, Y. Wang, J. Guo, X. Qiu, Z. Zeng, L. Jiang, S. Yi, S. Watanabe, L. Liao, Y. Bai, T.-Q. Nguyen, Y. Hu, *Adv. Sci.* **2022**, *9*, 2203111.

[18] a) J. F. Ponder Jr., S. A. Gregory, A. Atassi, A. K. Menon, A. W. Lang, L. R. Savagian, J. R. Reynolds, S. K. Yee, *J. Am. Chem. Soc.* **2022**, *144*, 1351; b) J. F. Ponder Jr., S. A. Gregory, A. Atassi, A. A. Advincula, J. M. Rinehart, G. Freychet, G. M. Su, S. K. Yee, J. R. Reynolds, *Angew. Chem., Int. Ed.* **2023**, *62*, 202211600; c) K. Janus, D. Chlebosz, A. Janke, W. Goldeman, A. Kiersnowski, *Macromolecules* **2023**, *56*, 964; d) J. Wu, X. Yin, F. Yang, S. Wang, Y. Liu, X. Mao, X. Nie, S. Yang, C. Gao, L. Wang, *Chem. Eng. J.* **2022**, *429*, 132354; e) S. Y. Son, Y. Kim, J. Lee, G. Y. Lee, W. T. Park, Y. Y. Noh, C. E. Park, T. Park, *J. Am. Chem. Soc.* **2016**, *138*, 8096.

[19] D. Venkateshvaran, M. Nikolka, A. Sadhanala, V. Lemaur, M. Zelazny, M. Kepa, M. Hurhangee, A. J. Kronemeijer, V. Pecunia, I. Nasrallah, I. Romanov, K. Broch, I. McCulloch, D. Emin, Y. Olivier, J. Cornil, D. Beljonne, H. Sirringhaus, *Nature* **2014**, *515*, 384.

[20] a) R. J. Kline, M. D. McGehee, E. N. Kadnikova, J. Liu, J. M. Fréchet, M. F. Toney, *Macromolecules* **2005**, *38*, 3312; b) S. Himmelberger, K. Vandewal, Z. Fei, M. Heeney, A. Salleo, *Macromolecules* **2014**, *47*, 7151.

[21] a) F. C. Spano, C. Silva, *Annu. Rev. Phys. Chem.* **2014**, *65*, 477; b) N. J. Hestand, F. C. Spano, *Chem. Rev.* **2018**, *118*, 7069.

[22] D. Neusser, C. Malacrida, M. Kern, Y. M. Gross, J. van Slageren, S. Ludwigs, *Chem. Mater.* **2020**, *32*, 6003.

[23] W. Liu, L. Müller, S. Ma, S. Barlow, S. R. Marder, W. Kowalsky, A. Köhn, R. Lovrincic, *J. Phys. Chem. C* **2018**, *122*, 27983.

[24] a) S. Himmelberger, A. Salleo, *MRS Commun.* **2015**, *5*, 383; b) R. Noriega, *Macromol. Rapid Commun.* **2018**, *39*, 1800096; c) S. Wang, *Synth. Met.* **2019**, *251*, 104; d) J. Chen, J. Yang, Y. Guo, Y. Liu, *Adv. Mater.* **2022**, *34*, 2104325; e) R. Dilmurat, V. Lemaur, Y. Olivier, S. M. Gali, D. Beljonne, *J. Phys. Chem. C* **2022**, *126*, 3118.

[25] R. A. Street, J. E. Northrup, A. Salleo, *Phys. Rev. B* **2005**, *71*, 165202.

[26] a) J. Mei, D. H. Kim, A. L. Ayzner, M. F. Toney, Z. Bao, *J. Am. Chem. Soc.* **2011**, *133*, 20130; b) T. Lei, J. H. Dou, J. Pei, *Adv. Mater.* **2012**, *24*, 6457; c) J. Kim, J. Guo, G. Sini, M. K. Sørensen, J. W. Andreasen, K. L. Woon, V. Coropceanu, S. H. K. Paleti, H. Wei, S. Peralta, M. Mallouki, C. Müller, Y. Hu, T.-T. Bui, S. Wang, *Mater. Today Adv.* **2023**,

18, 100360; d) M. Li, C. An, W. Pisula, K. Müllen, *Acc. Chem. Res.* **2018**, *51*, 1196; e) J. Kim, X. Ren, Y. Zhang, D. Fazzi, S. Manikandan, J. W. Andreasen, X. Sun, S. Ursel, H.-I. Un, S. Peralta, M. Xiao, J. Town, A. Marathianos, S. Roesner, T.-T. Bui, S. Ludwigs, H. Sirringhaus, S. Wang, *Adv. Sci.* **2023**, *10*, 2303837; f) X. Cao, H. Li, J. Hu, H. Tian, Y. Han, B. Meng, J. Liu, L. Wang, *Angew. Chem., Int. Ed.* **2023**, *62*, 202212979.

[27] I. E. Jacobs, C. Cendra, T. F. Harrelson, Z. I. Bedolla Valdez, R. Faller, A. Salleo, A. J. Moulé, *Mater. Horiz.* **2018**, *5*, 655.

[28] W. A. Wood, I. E. Jacobs, L. J. Spalek, Y. Huang, C. Chen, X. Ren, H. Sirringhaus, *Phys. Rev. Mater.* **2023**, *7*, 034603.